Hindawi
Advances in Civil Engineering
Volume 2023, Article ID 6251962, 19 pages
https://doi.org/10.1155/2023/6251962

Research Article

Fluid Vibration Analysis of Large-Span Skeletal Membrane Structures under Pulsating Winds

Wei Fu, Haixu Yang, and Jie Jia

School of Civil Engineering, Northeast Forestry University, Harbin 150040, China

Correspondence should be addressed to Haixu Yang; yhxcumt@163.com

Received 3 March 2023; Revised 22 May 2023; Accepted 29 May 2023; Published 22 July 2023

Academic Editor: Tianshou Ma

To identify the location of the strongest vibration of skeletal membrane structures under pulsating wind and predict the response and damage of the structures. To guide engineering reinforcement, base on the platform of ANSYS Workbench as a platform, the complex skeleton membrane structure is first simplified using the modal fitting method, and the error of the 30th-order frequency of the membrane structure before and after the simplification is calculated to be less than 5% compared to the unsimplified model. Based on the simplified model, the unidirectional coupling and bidirectional coupling methods were compared using the surface averaging wind pressure distribution parameters of the membrane structure. The results show that the extreme value and extreme difference of the averaged wind pressure of the bidirectional coupling are larger than those of the unidirectional coupling under the same wind angle, which verifies the reliability of the vibration analysis of the large-span membrane structure under the bidirectional coupling. By analyzing the wind pressure coefficients at the key measure points, it can be seen that the structure is in unfavorable working condition at the wind angle of 0°–45°. Based on the bidirectional coupling method, the maximum displacement time variation curve, maximum acceleration time variation curve, and maximum equivalent force time variation curve for different wind direction angles are basically the same, and the membrane structure gradually equilibrates with time, and the maximum instantaneous displacement, maximum instantaneous acceleration, and maximum equivalent force all reach the maximum at wind direction angle 30° and the minimum at 90°.

1. Introduction

With the continuous development of science and technology, the application of large span membrane structures is widely used [1, 2]. The main body of a skeleton membrane structure is a steel member or various types of material support as a spatial structural support, whereas the membrane material is covered on the support as an envelope structure, so that the membrane material and the skeleton form a jointly stressed structural system. Most membrane materials have the characteristics of lightness, softness, low stiffness, and damping, while exhibiting significant geometric nonlinearities [3]. The pulsating wind has the characteristic of changing randomly over time, so when the vibration frequency of the structure is close to the natural frequency of the membrane structure, resonance will occur and the membrane structure under the pulsating wind load is prone to wind vibration [4–6]. As the wind direction changes, the distribution of wind pressure on the surface of the structure has a significant impact, which affects the stability of the structure. In practice, most skeletal membrane structures do not take into account the wind-induced response under the joint action of fluctuating wind and fluid-solid coupling; therefore, it is necessary to analyze the wind-induced response of fluctuating wind under fluid-solid coupling. Because the correlation between the pulsating components of the natural wind in the X, Y, Z directions is weak, and the horizontal and vertical wind directions have less influence on the structure, this paper is based on computational fluid dynamics (CFD) and computational structural dynamics (CSD) techniques to study the transient response of pulsating wind skeleton membrane structures with different wind angles downwind.

In terms of model simplification, He et al. [7] proposed a fitting modal method for dynamic modeling. The modes calculated by large-scale finite element analysis software were fitted into polynomial forms to obtain an approximate

analytical expression for the curved beam modes, simplifying the modeling and calculation process. Wu et al. [8] conducted simplified and dynamic analysis on large satellite structures using beam modeling method, additional mass method, RBE3-mass modeling method, and virtual mass method, and Mazzilli et al. [9] provide an extensive survey of scholarly literature regarding nonlinear modes of vibration and their significance in generating more effective reduced-order models.

In terms of dynamic analysis, Pan et al. [10] obtained from the study of the vibration frequency characteristics of open and closed films under incoming wind that the additional mass is the main factor affecting the vibration frequency of film structures, and the effect of air-bearing stiffness on the vibration frequency of closed films cannot be ignored. Zhang et al. [11] found that when the film prestress is less than the critical value, the vibration of the film structure is dominated by the film, and when the film prestress is greater than the critical value, the film and the frame are coupled to vibrate. Rong et al. [12] analyzed the kinetic energy change of the thin film space structure system to study its motion process and unfolding stability. It can be found that the kinetic properties of the thin film space structure are affected by different modes of motion; the smaller the unfolding rate of the thin film structure, the better the unfolding stability. Wu et al. [13] studied the aeroelastic instability characteristics and mechanism of two closed-type saddle shaped tensioned membrane structures by wind tunnel test, for most wind directions, several vibration modes are excited and the amplitude and damping ratio of the roof slowly increase with the oncoming flow velocity. Sun et al. [14] investigated the effects of lateral pulsating winds at different wind speeds on the wind-induced vibration response and wind pressure distribution of different membrane structures.

The current algorithm for solving fluid–solid coupling is weak coupling [15, 16], in which two-way fluid–solid coupling combines CFD and computational solid mechanics (CSD) to calculate the stress and strain of solids under the action of fluids and the flow-field changes of fluids under the influence of solid deformation. The one-way fluid–solid coupling only considers the stress and strain of the solid under the action of the fluid. Chen et al. [17] realized single and bidirectional fluid–solid coupling through CFD and finite-element methods, and took the cantilever plate as the research object to calculate the vibration response characteristics and hydrodynamic characteristics of the cantilever plate under different Reynolds numbers, to capture the vortex induced resonance phenomenon. Lu et al. [18] and Sun and Gu [19] studied the fluid-structure interaction (FSI) of membrane structures under wind actions by novel numerical method, and obtained some significant results for the wind-resistant design ofmembrane structures. The fluid–solid coupling numerical simulation is carried out, and the displacement response time history of the structure is obtained.

In this paper, the vibration form of the structure is predicted by modal analysis, and the consistency of the vibration before and after simplification is ensured by the modal fitting method. The stability of the structure is further analyzed by combining wind pressure and wind vibration response analysis with wind pressure coefficient values and parameters such as maximum displacement, maximum acceleration, and maximum equivalent force values.

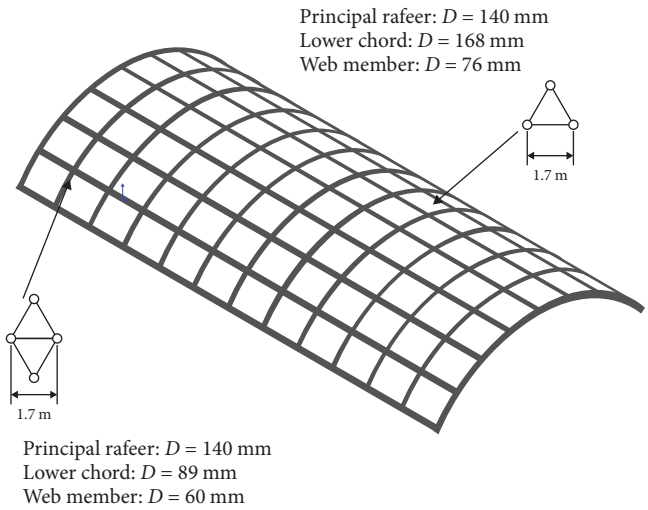

Figure 1: Diagram of coal shed model.

2. Model and Methods

2.1. Computational Model. The calculation model of this paper is a coal shed in Shanxi as shown in Figure 1, the membrane structure part of this coal shed adopts 1.0 mm thick PTFE material, the steel structure adopts Q345B steel, the structural parameters are detailed in Table 1. The upper string uses $\varphi 140 \times 6$, the lower string uses $\varphi 168 \times 6$, the oblique belly rod uses $\varphi 76 \times 4$, the upper straight belly rod uses rectangular section, which size is $140 \times 80 \times 3 \times 3$, the chord oblique web bar uses $\varphi 114 \times 4$ in the main truss. The upper chord of the secondary truss uses $\varphi 114 \times 4$ the lower string uses $\varphi 89 \times 4$, the oblique belly rod uses $\varphi 60 \times 3$, the upper oblique belly rod uses $\varphi 76 \times 3$ in the secondary truss. The sagittal span ratio of main truss is 1/4, the height of arch section is 1/35, the overall span is 84 m, the length is 171 m, and the total construction area is 14,553.25 m^2. The structure satisfies the Code for Structural Loads of Buildings (GB50009-2012) [20], Technical Specification for Membrane Structure (CECS158-2015) [21], and Design Standard for Steel Structure (GB50017-2017) [22] design requirements.

The wind vibration response analysis of structural is different from the static analysis, and the membrane structure and the main structure must be analyzed as a whole, because the dynamic characteristics of the membrane structure will be essentially changed after it is separated out, and the existence of a large number of steel structures can not accurately predict the vibration situation because of the fluid–solid coupling analysis of wind vibration response, and the achievability is lower. The steel structure is considered to be simplified, and the steel structure is projected onto the surface of the membrane structure according to the position relationship, and the simplified model is shown in Figure 2. Ultimately, it is inevitable to consider reducing the differences

Table 1: Basic setup of membrane structure.

Membrane material parameters	Modulus of elasticity (N/mm^2)	Poisson's ratio	Tensile stiffness (KN/m)	Pre-tension (KN/m)	Shear modulus (N/mm^2)
	1,400	0.35	1,400	3	400
Steel parameters	Elastic modulus (N/mm^2)	Poisson's ratio	Coefficient of linear expansion	Mass density (kg/m^3)	Shear modulus (N/mm^2)
	2.06×10^5	0.3	1.25×10^5	7,850	7.92×10^4

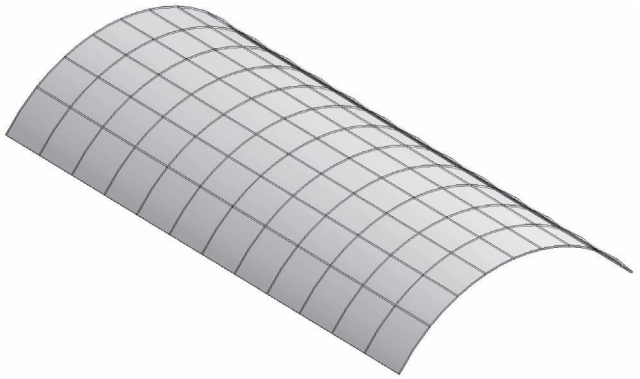

Figure 2: Simplified diagram of coal shed.

of the model simplification, and the simplified model is adjusted and measured in certain tension, mass block and constraint position, so that its modal first 30 order frequencies and the modal frequencies of the model before simplification are consistent under certain errors, and this method is called the modal fitting analysis of dynamics basis. The effect of the bottom structure on the membrane structure has been incorporated into the calculation by means of a simplified fitting.

2.2. Model Simplification Reliability Analysis. Modal analysis is a basic method to study the vibration properties of a structure. Its purpose is to identify the modal parameters of a vibrating system and provide a basis for vibration analysis and optimization of the dynamic properties of the structure. The frequencies of each order before and after model simplification keep the same trend under certain errors. It can show that the inherent vibration properties of the model are not affected by the simplification, which provides a physical model basis for wind-induced vibration analysis. Modal vibration equation:

$$[M]\{\ddot{y}(t)\} + [C]\{\dot{y}(t)\} + [K]\{y(t)\} = 0. \quad (1)$$

In Equation (1), $[M]$ is the mass matrix, $[C]$ is the damping matrix, and $[K]$ is the stiffness matrix. By adjusting the mass, damping, and stiffness terms, the frequencies are fitted for the model simplification. For the simplified model, the prestress modal analysis method is used to consider the large deformation effect under tension. The frequency-distribution curves of the first 30 orders of modal before and after the model simplification are shown in Figure 3(a). In Figure 3(a), a small range of frequency step situation occurs after the 10th order. Figure 4 gives a comparison vibration cloud of the 9th–12th order, for which the 10th order local vibration turns into the

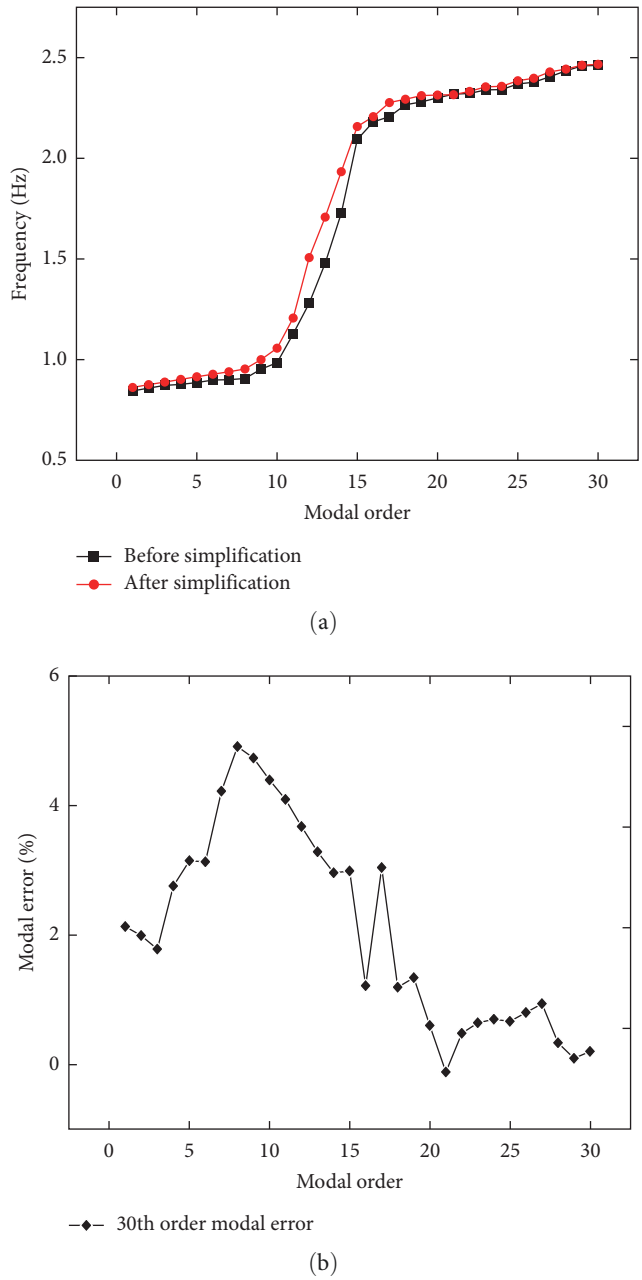

Figure 3: Diagram of modal frequency and error distribution. (a) Modal frequency distribution. (b) Error distribution of each order.

11th order overall offset leading to the step phenomenon. The frequency error of each order before and after the model simplification is shown in Figure 3(b) curve with a maximum error of about 5%, which well ensures the consistency of the

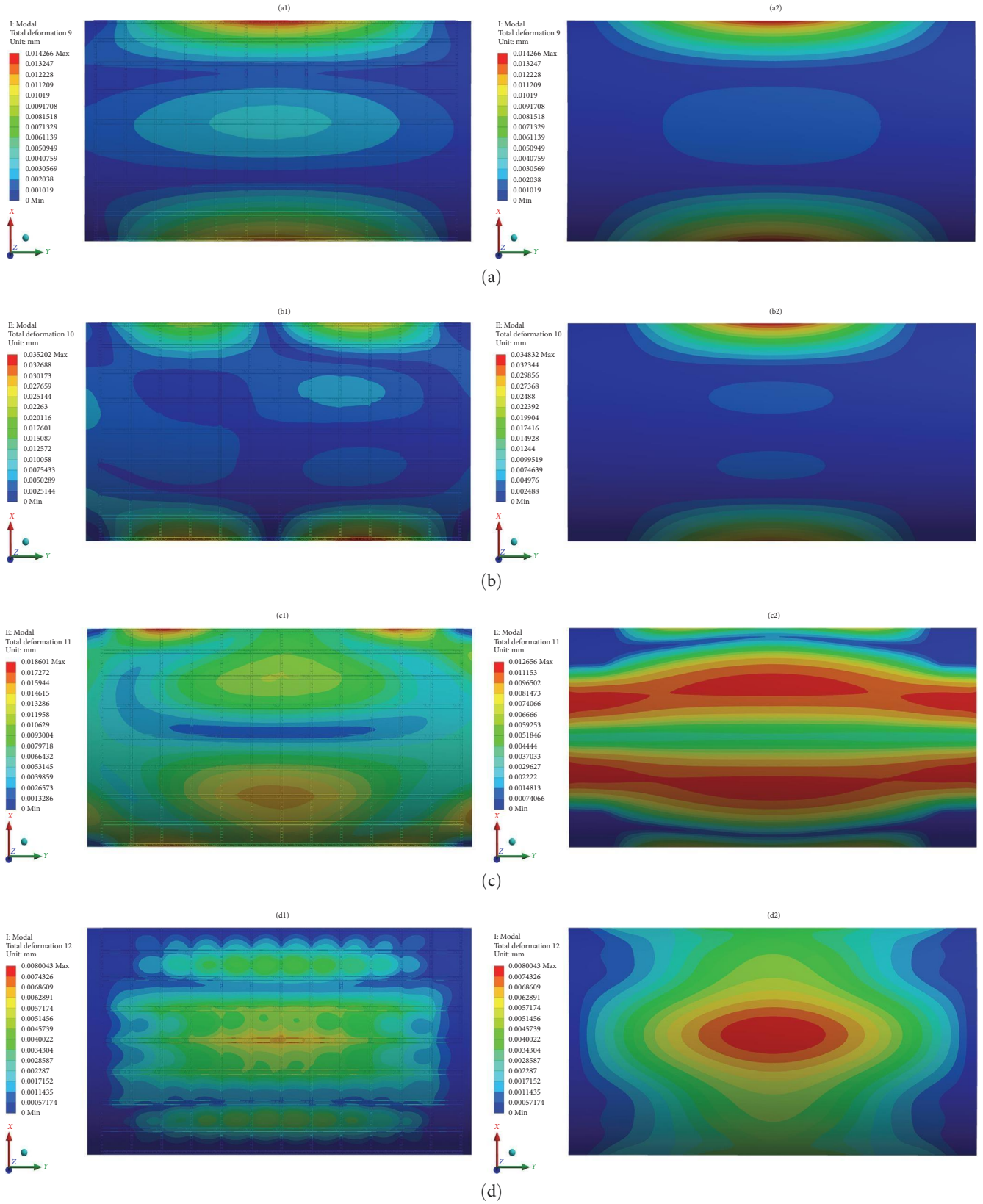

FIGURE 4: Membrane structure mode nephogram. (a1)–(a2) 9th order vibration cloud diagram. (b1)–(b2) 10th order vibration cloud diagram. (c1)–(c2) 11th order vibration cloud diagram. (d1)–(d2) 12th order vibration cloud diagram.

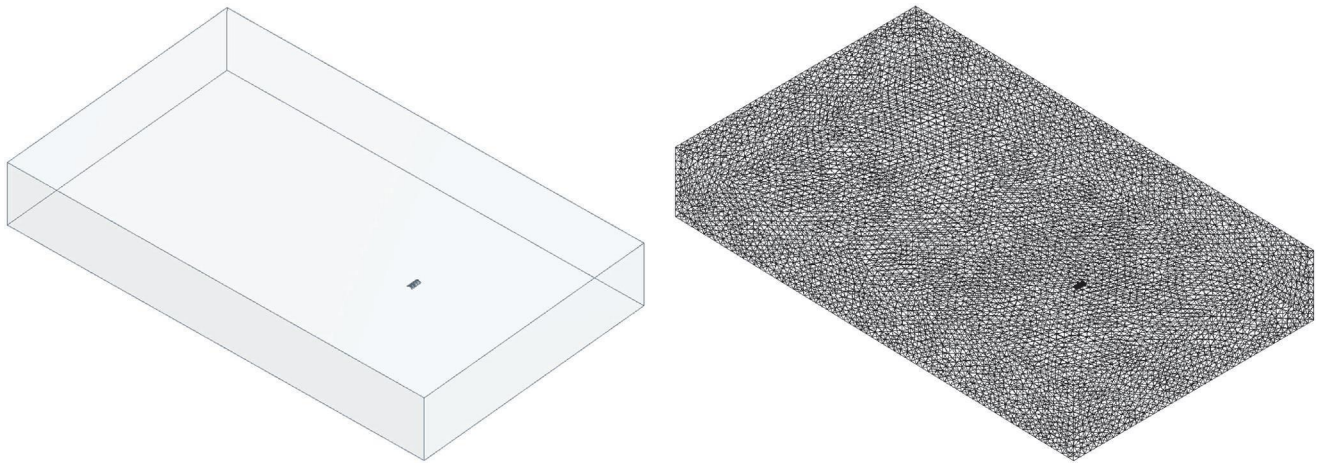

(a) (b)

Figure 5: Diagram of simulation model. (a) Fluid domain model. (b) Grid model.

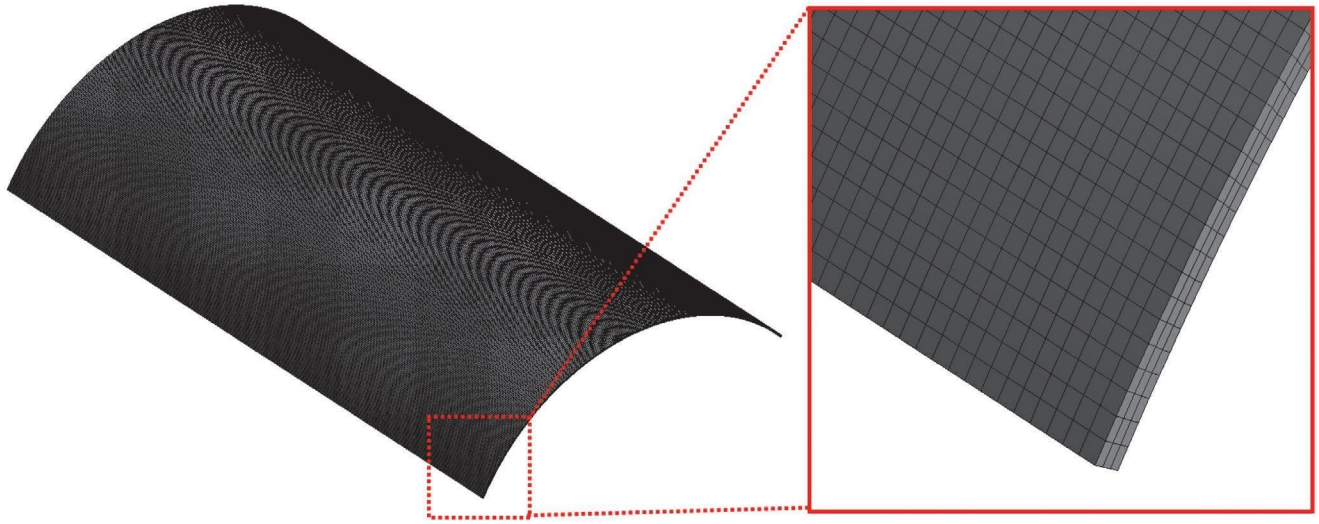

(a) (b)

Figure 6: Diagram of Structural model grid. (a) Overall mesh model, (b) local grid schematic.

vibration characteristics before and after the model simplification. To better ensure consistency in the vibration characteristics of the model before and after simplification, Figure 4 also presents the fitted mode shapes of the structure for the 9th–12th orders before and after simplification.

3. Model Parameters and Boundary Conditions

3.1. Fluid Domain Settings. When performing numerical fluid simulation, the computational domain is set up to simulate an infinite flow-field region with a finite flow field. To ensure the validity of the calculation, the fluid domain obstruction ratio requirement needs to be satisfied [23], and the rectangular wind field domain size of 2,565 m × 1,260 m × 120 m is established with an open-period boundary around it, and the ground is closed-wall surface considering the roughness, and the ground roughness is B class site ground [20], as shown in Figure 5(a). The grid discretization of the fluid domain is carried out, and the number of grid cells is 5,512,000; the number of grid nodes is 3,055,000; and the grid mass is more than 0.418; and the grid model is shown in Figure 5(b).

3.2. Structured Domain Settings. The structural domain model is meshed discretized with MultiZone mesh type as shown in Figure 6(a), and due to the thin film thickness, at least two layers of mesh in the thickness direction must be ensured as shown in Figure 6(b). The number of grid cells is 338,000; the number of grid nodes is 1,697,000; and the grid model is shown in Figure 6.

3.3. Boundary Conditions. In this study, $Re = U\ \rho\ L/\mu = 3.403 \times 10^8$, where U is taken as the maximum wind speed of the pulsating wind, ρ is the air density, L is the characteristic length of the fluid, and μ is the dynamic viscosity coefficient of the fluid. Because the Re value belongs to high Reynolds number, and to conserve computing resources, the Realizable k-$\mathcal{E}$ turbulence model in the time-homogenized Reynolds equation

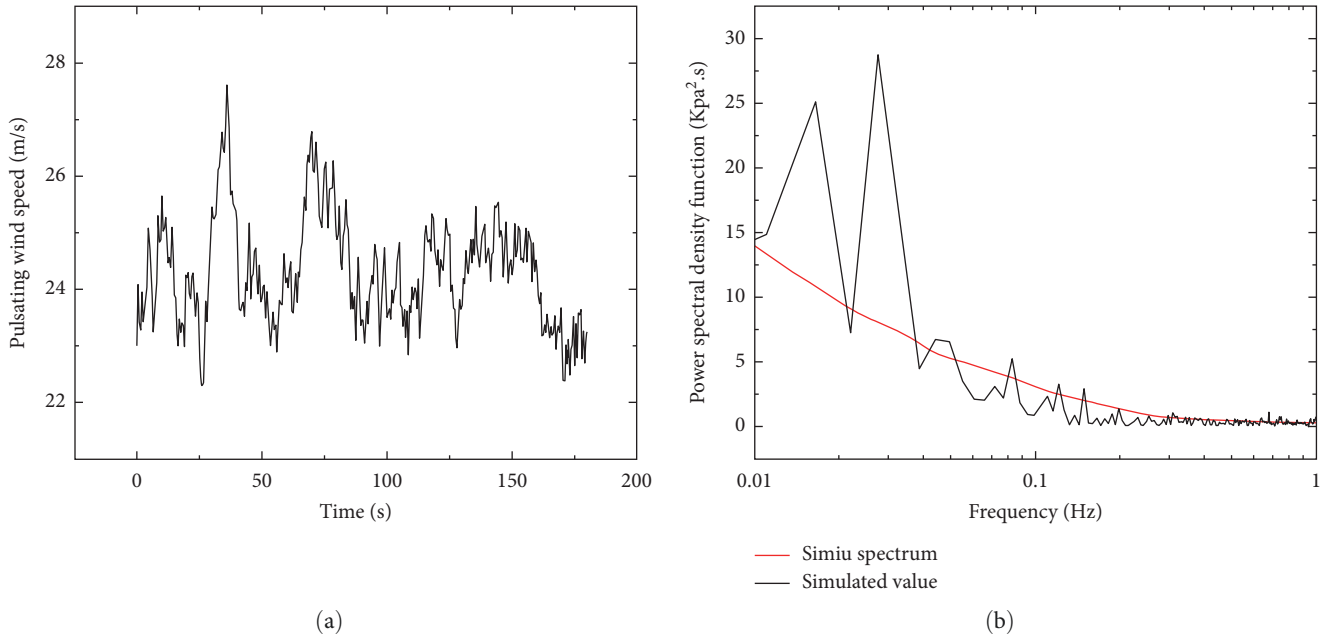

Figure 7: Diagram of pulsating wind. (a) Pulsating wind speed time course curve. (b) simiu wind speed spectrum.

averaging (RANS) method is selected. In this study, the inlet wind velocity is discrete time-dependent pulsating wind data, and the pulsating wind data are referenced from [24] with certain transformations. The User-Defined Function (UDF) of FLUENT, that is, UDF is used to write dynamic links to the solver using C language. The UDF header file #include "udf.h" was defined and the discrete data points were loaded into the program by compiling Complied using the DEFINE_PROFILE (unsteady_vel,t,i) macro language with the entrance velocity setting UDF program with the bottom boundary set to wall and 0.15 according to the wall roughness [20]. The discrete pulsating wind data are obtained after fitting as shown in Figure 7(a), and the Simiu power spectrum distribution is obtained after FFT transformation of the time-range wind speed data Figure 7(b), the pulsating wind load frequency is concentrated in the low-frequency band, which coincides with the vibration property frequency of the structure in the above study and can better analyze the vibration of the structure.

3.4. Finite-Element Verification. To ensure the reliability of the calculation results, this article is conducting irrelevance verification of the computational domain grid. With respect to the wind direction angle of 0°, the wind pressure coefficient of monitoring point 17 is obtained, as shown in the trend results in Figure 8. The results indicate that as the number of grids increases, the wind pressure coefficient of measuring point 17 shows a trend of increasing and then stabilizing. The data error decreases as the number of grids increases from 5,512,346, and as the number of grids increases from 5,512,346 to 11,024,114, which is close to twice the original number, the difference in results is only 0.82%. To be more convincing, the parameters of measuring points 1 and 15 are also given, and the relationship between the number of grids and the wind pressure coefficient is shown in

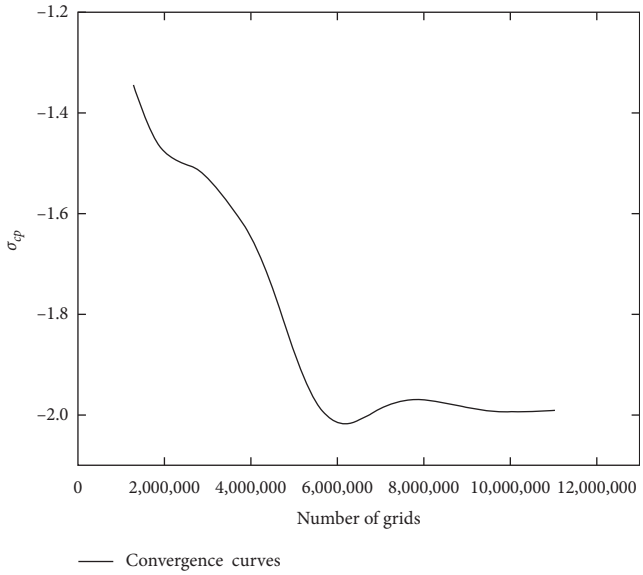

Figure 8: Mesh irrelevance verification convergence curve.

Table 2. Therefore, considering the issue of computational resources, 5,512,346 grids are selected for subsequent analysis.

The parameter settings in this study are strictly referenced from the literature [25]. The model used in this literature study is similar to the model studied in this paper, and the specific wind pressure coefficients derived from the wind tunnel experiments are similar to the numerical simulation results in this study. The accuracy of the numerical simulations in this paper can be verified.

4. Analysis of Calculation Results

In this study, the main research variable is the wind angle [26], which is taken as 0°, 15°, 30°, 45°, 60°, 75°, and 90°,

Table 2: Grid volume irrelevance verification.

Number of grids	Measurement point 1	Measurement point 15	Measurement point 17
1,287,159	0.54	0.65	−1.34
1,715,921	0.58	0.70	−1.44
2,789,783	0.62	0.87	−1.51
3,402,189	0.64	0.90	−1.57
4,161,251	0.71	0.94	−1.67
5,512,346	0.73	1.03	−1.97
7,154,612	0.73	1.04	−1.98
9,215,145	0.73	1.05	−1.98
11,024,114	0.73	1.06	−1.99

Table 3: Summary of extreme values of wind pressure coefficients for rigid and flexible.

Coupling type		0°	15°	30°	45°	60°	75°	90°
Unidirectional	Positive pressure	1.15	1.20	1.18	1.08	0.95	0.98	0.99
	Negative pressure	2.25	2.31	3.10	3.63	2.64	2.65	1.28
	Difference value	3.40	3.51	4.28	4.71	3.59	3.63	2.27
Bidirectional	Positive pressure	2.60	1.86	1.93	1.85	1.95	1.74	1.75
	Negative pressure	2.27	3.32	3.41	3.25	2.44	3.03	1,32
	Difference value	4.87	5.18	5.34	5.1	4.39	4.77	3.07

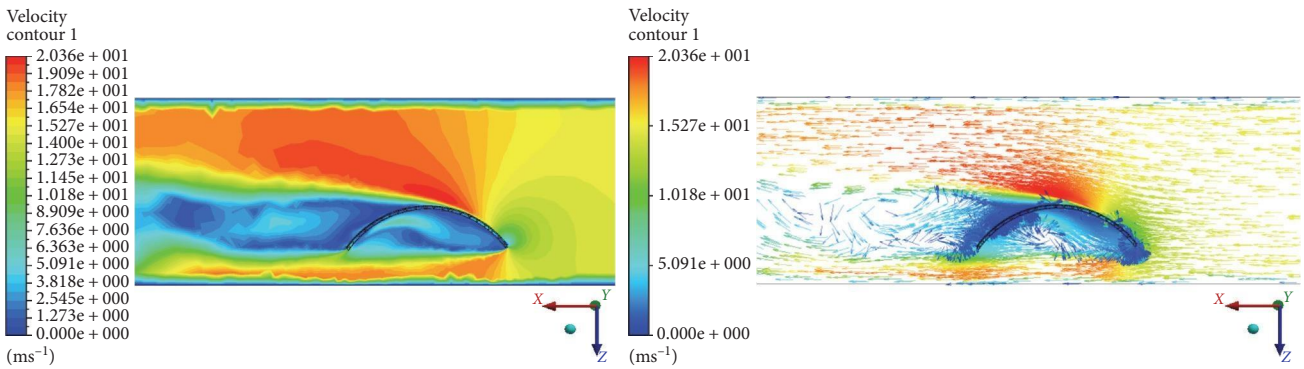

Figure 9: Diagram of cross-section velocity.

whereas the distribution of wind pressure in membrane structures with different wind angles and the vibration response values generated on the membrane surface under the action of pulsating wind with different wind angles are calculated using unidirectional coupling and bidirectional coupling methods.

4.1. Comparative Analysis of the Distribution of Averaged Wind Pressure Coefficients. Table 3 gives the extreme values of wind pressure coefficient distribution and the difference between positive and negative pressure wind pressure coefficients for unidirectional coupling and bidirectional coupling film surface averaging. The difference of wind pressure coefficient reflects the comprehensive degree of the structure under tension and pressure, and the larger the difference, the more obvious the structure is "torn" and the more easily the structure is destroyed. The maximum difference value of unidirectional coupling appears at the wind direction angle of 45°, the maximum difference value is 4.71, and the minimum difference value appears at the wind direction angle of 90°, the minimum difference value is 2.27; the maximum difference value of bidirectional coupling appears at 30°, the maximum difference value is 5.34, and the minimum difference value also appears at the wind direction angle of 90°, the minimum difference value is 3.07; both unidirectional coupling and bidirectional coupling wind pressure coefficient difference values show the wind direction from 0° to 90°, first the wind pressure coefficient is 3.07. The difference of wind pressure coefficients of both unidirectional and bidirectional coupling shows a trend of increasing and then decreasing from wind direction angle 0° to 90°, which is basically consistent with the law in the literature [27]; in addition, because the bidirectional coupling also considers the influence of solid deformation on the flow field, which leads to stronger vibration of the membrane structure and makes the difference of wind pressure coefficients of each wind direction angle larger than that of unidirectional coupling.

Comprehensive Figures 9 and 10 can be found that the structure surface will produce negative pressure effect, according to Bernoulli's principle, at this time the pressure is the

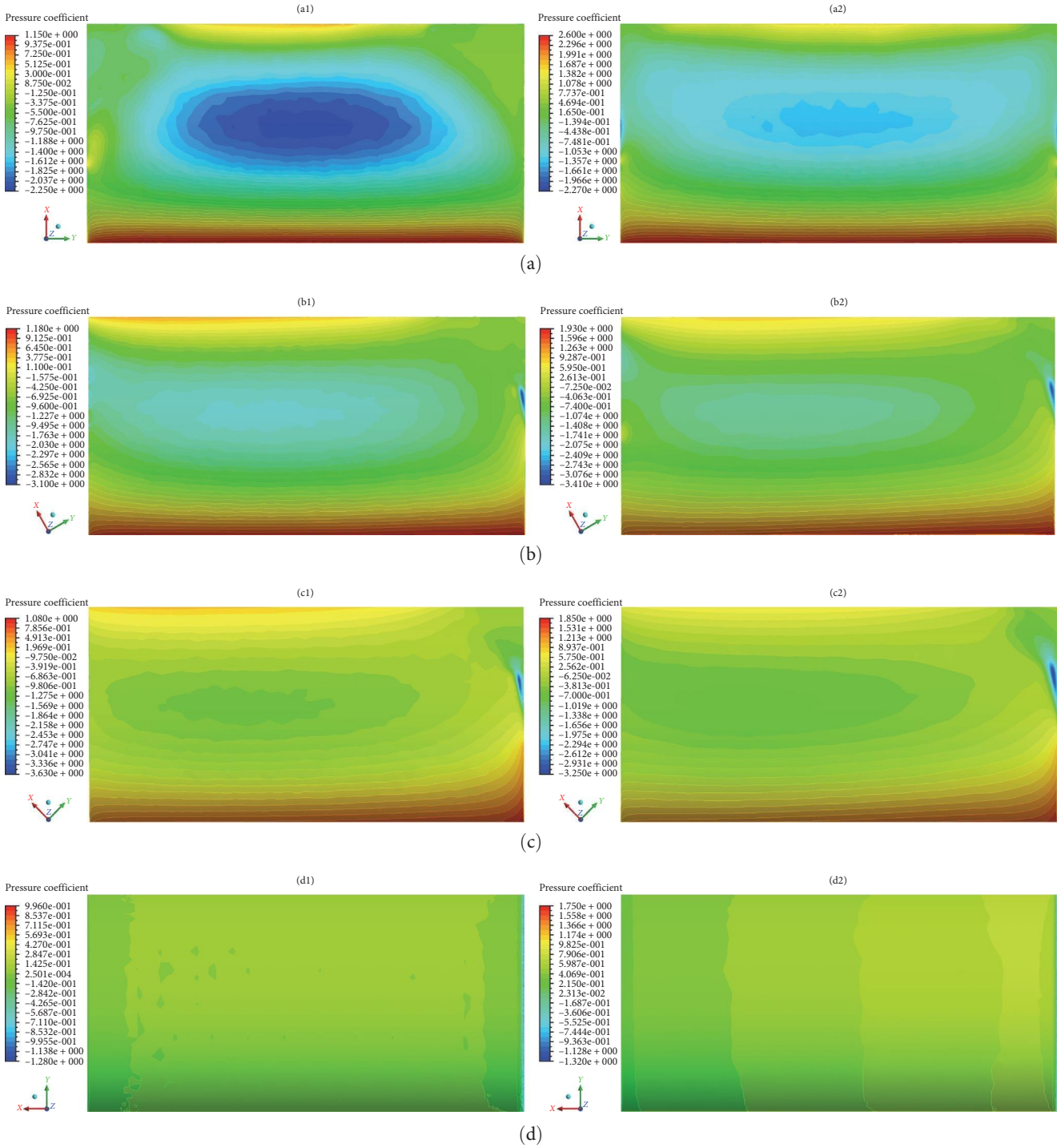

Figure 10: Wind pressure distribution of rigid and flexible structures. (a1) 0° wind angle unidirectional. (a2) 0° wind angle bidirectional. (b1) 30° wind angle unidirectional. (b2) 30° wind angle bidirectional. (c1) 45° wind angle unidirectional. (c2) 45° wind angle bidirectional. (d1) 90° wind angle unidirectional. (d2) 90° wind angle bidirectional.

smallest, and the edge of the membrane in the leeward area is subject to the simultaneous action of the upper and lower airflow, which makes the winded area produce a winding effect and a positive pressure effect locally, and the leeward area is prone to a stronger vibration under the action of the pulsating wind. Figure 9 gives a cloud diagram of the wind pressure coefficient distribution at 0°, 30°, 45°, and 90° for the unidirectional coupling and bidirectional coupling wind angles, and the distribution trend law is also basically consistent with that in the literature [27], and the distribution of wind pressure coefficients at different wind angles shows an overall gradually shifting trend. From the distribution of wind pressure

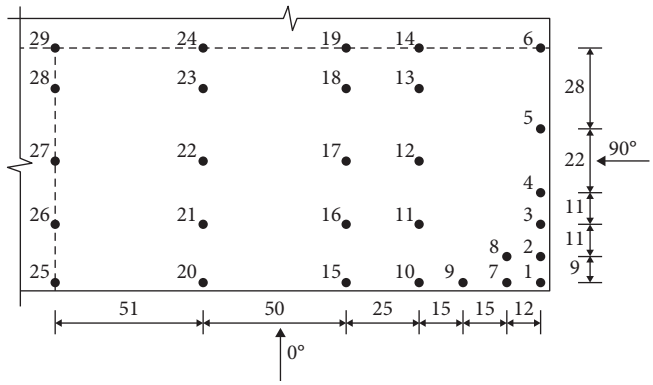

Figure 11: Typical wind pressure measurement point number.

coefficient, it can be seen that the trend of wind pressure distribution between unidirectional coupling and bidirectional coupling is basically the same; the maximum pulsating positive pressure will be generated at the edge of the windward side, and the airflow moves upward along the membrane surface, and the velocity reaches the maximum when the airflow reaches the top.

To describe the distribution of the averaged wind pressure coefficient on the surface of the membrane structure in more detail, typical measurement points [27] 1, 2, and 7 at the corner of the model, typical measurement points 4, 5, and 15 at the edge, and typical measurement points 17, 19, and 27 at the middle were selected for comparative analysis, and the numbering arrangement of the measurement points is shown in Figure 11.

From Figure 12, it can be found that in the corner area, the pulsation averaged wind pressure coefficient of the unidirectional coupling surface measurement point increases slightly with the wind direction angle and then decreases, and the pulsation averaged wind pressure coefficient of the bidirectional coupling surface measurement point is smaller overall with the increase of the wind direction angle. The maximum pulsation wind pressure coefficient is 1.15 and 2.59 at measurement point 7, indicating that the most unfavorable working condition in the corner area is 0° wind angle, when the downforce generated by bidirectional coupling is greater than that of unidirectional coupling.

The pulsation-averaged wind pressure coefficient of the unidirectional coupling surface measurement point 4 in the right edge region increases with the wind direction angle, whereas the bidirectional coupling results vary irregularly, and the maximum values of the pulsation-averaged wind pressure coefficients for both are −0.38 and 0.89 at the 0° wind direction angle, indicating that the region is also most unfavorable at the 0° wind direction angle, and shows different forms of deformation. For measurement point 5, the maximum pulsation-averaged wind pressure coefficient for the unidirectional coupling is −3.15, which occurs at a 45° wind direction angle. The maximum pulsation averaging wind pressure coefficient out of the position of measurement point 5 for the bidirectional coupled surface is −2.07, which occurs at 30° wind angle. It can be found that the unfavorable conditions at the right edge of the structure are concentrated in the wind direction angles from 0° to 45°. The maximum pulsation averaging wind pressure coefficients of 1.02 and 2.59 for the unidirectional coupling and bidirectional coupling measurement point 15 occur at 15° and 0° wind angles, respectively, indicating that the most unfavorable wind angles in the lower edge area are from 0° to 15° wind angles.

The maximum pulsation-averaged wind pressure coefficients at the central region for unidirectional and bidirectional coupled surfaces were −2.13 and −1.5 for measurement point 17, both occurring at 15° wind angle, respectively, and 0.32 and 1.13 for measurement point 19, occurring at 30° and 0° wind angle, respectively, and −1.17 and −0.99, which occurred at 30° and 15° wind angles, respectively. This indicates that the most unfavorable wind angle in the middle region is in the wind angle of 0°–30°.

In summary, it can be found that during the whole analysis of the averaged wind pressure coefficient, the structure is most dangerous at the wind angle of 0°–45°, and the overall value of the pulsating averaged wind pressure coefficient for bidirectional coupling is greater than that of unidirectional coupling, and the wind pressure distribution on the membrane surface will be different under different coupling types, further verifying that the wind pressure distribution on the membrane surface will change significantly when considering the influence of membrane surface deformation on the flow field, that is, bidirectional coupling.

4.2. Comparative Analysis of Wind-Driven Vibration on Membrane Surface. After comparing the distribution of the averaged wind pressure coefficient on the membrane surface, the vibration of the membrane structure at typical wind angles of 0°, 30°, 45°, and 90° was compared and analyzed on the basis of bidirectional coupling, and the time course change curves of the maximum displacement of the membrane structure are given in Figure 13, the time course change curve of the maximum acceleration is given in Figure 14, and the time course curve of the maximum equivalent force is given in Figure 15. It can be seen that the trends of maximum displacement time range and maximum acceleration time range of maximum stress time range for different wind angles are basically the same, the moments of maximum displacement

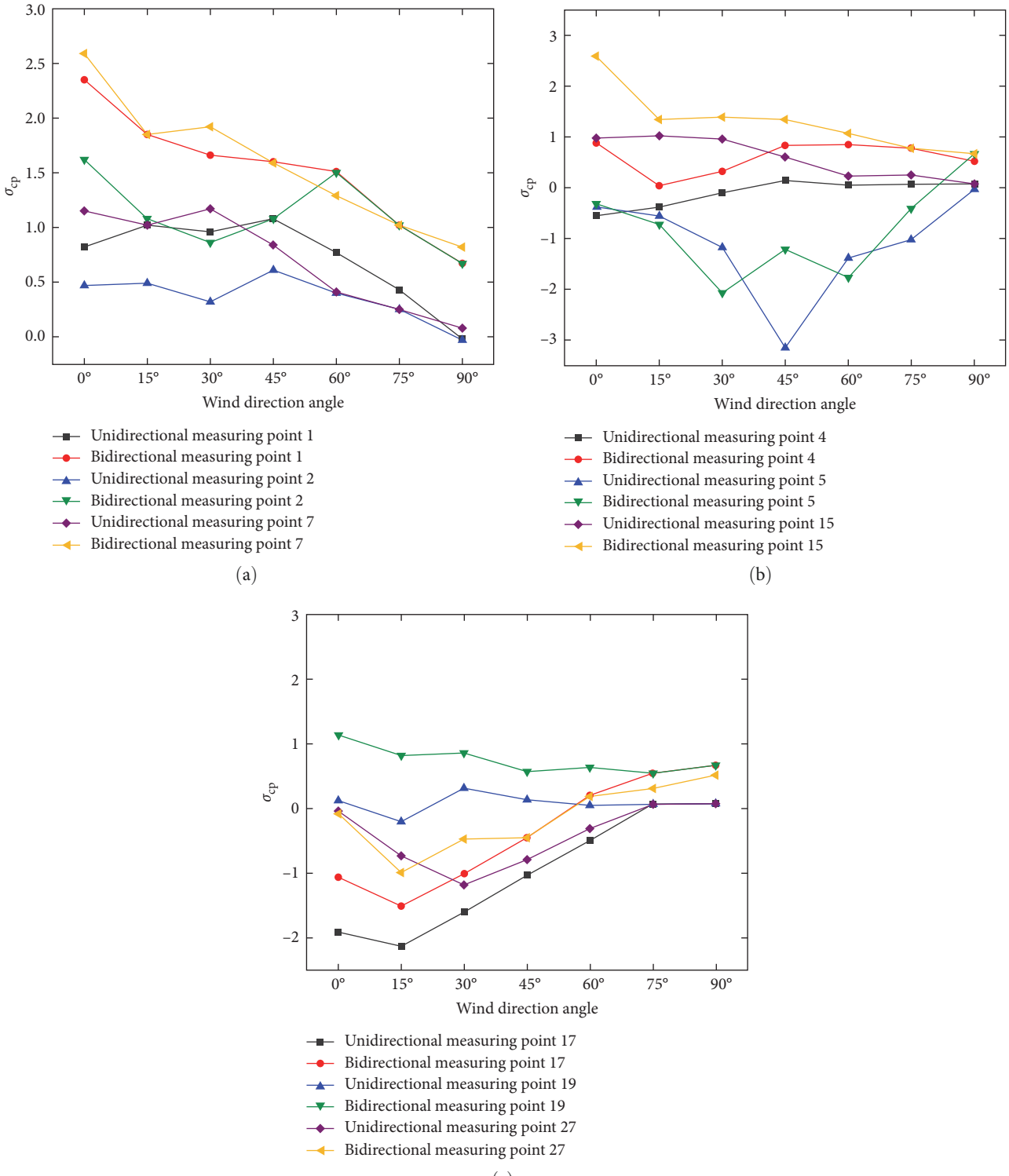

Figure 12: Variation curve of pulsating wind pressure coefficient with wind direction angle at key measurement points. (a) Corner measurement point wind pressure coefficient. (b) Edge measurement point wind pressure coefficient. (c) Central measurement point wind pressure coefficient.

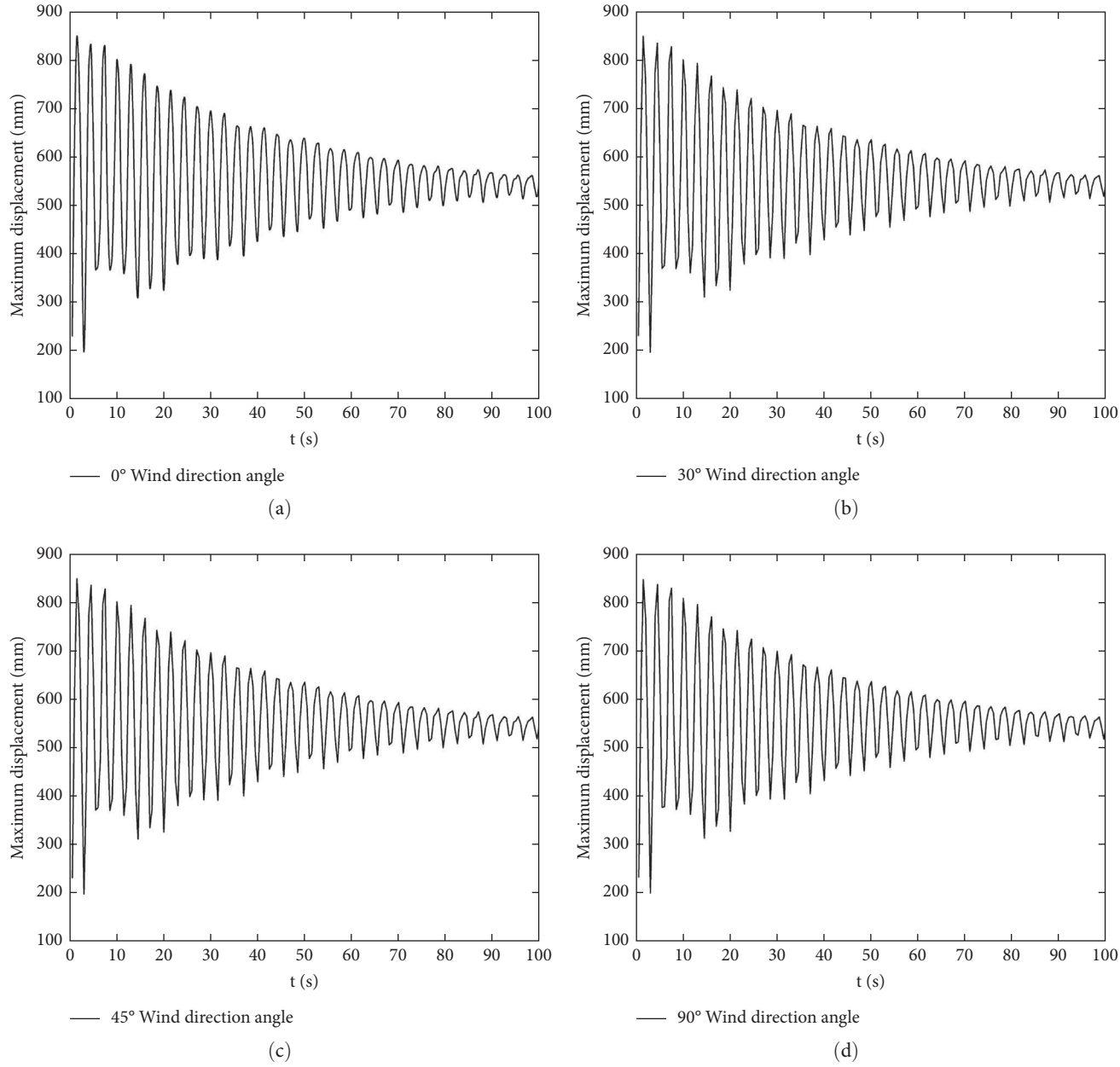

Figure 13: Diagram of time history curve of maximum equivalent stress of membrane structure (a) 0° wind direction angle. (b) 30° wind direction angle. (c) 45° wind direction angle. (d) 90° wind direction angle.

generated by different wind angles are all in the 1.5 s, the moments of maximum acceleration are all in the 2 s, and the maximum equivalent stresses are all in the 1 s. The possibility of convergence of the overall vibration of the structure over time, that is, the vibration amplitude is getting smaller, is due to the frequency distribution of the pulsating wind and the modal frequency of the membrane structure are within an order of magnitude, leading to a relatively strong structural vibration at the beginning. Combined with the flow velocity distribution of the wind pressure analysis above, the membrane structure belongs to the wind field around the flow state, and as time passes, the vortex behind the membrane structure gradually stabilizes and produces a certain effective effect, which makes the membrane structure gradually converge to equilibrium.

To more intuitively reflect the changes of wind vibration response values of the structure under the action of different pulsating wind angles, the maximum displacement cloud diagram is given in Figure 16, the maximum acceleration variation cloud diagram in Figure 17, and the maximum equivalent force cloud diagram in Figure 18, it can be seen that the maximum displacement, maximum acceleration, and maximum equivalent force of the structure under different wind angles are mainly reflected in the differences of distribution at different locations, and the overall displacement, acceleration,

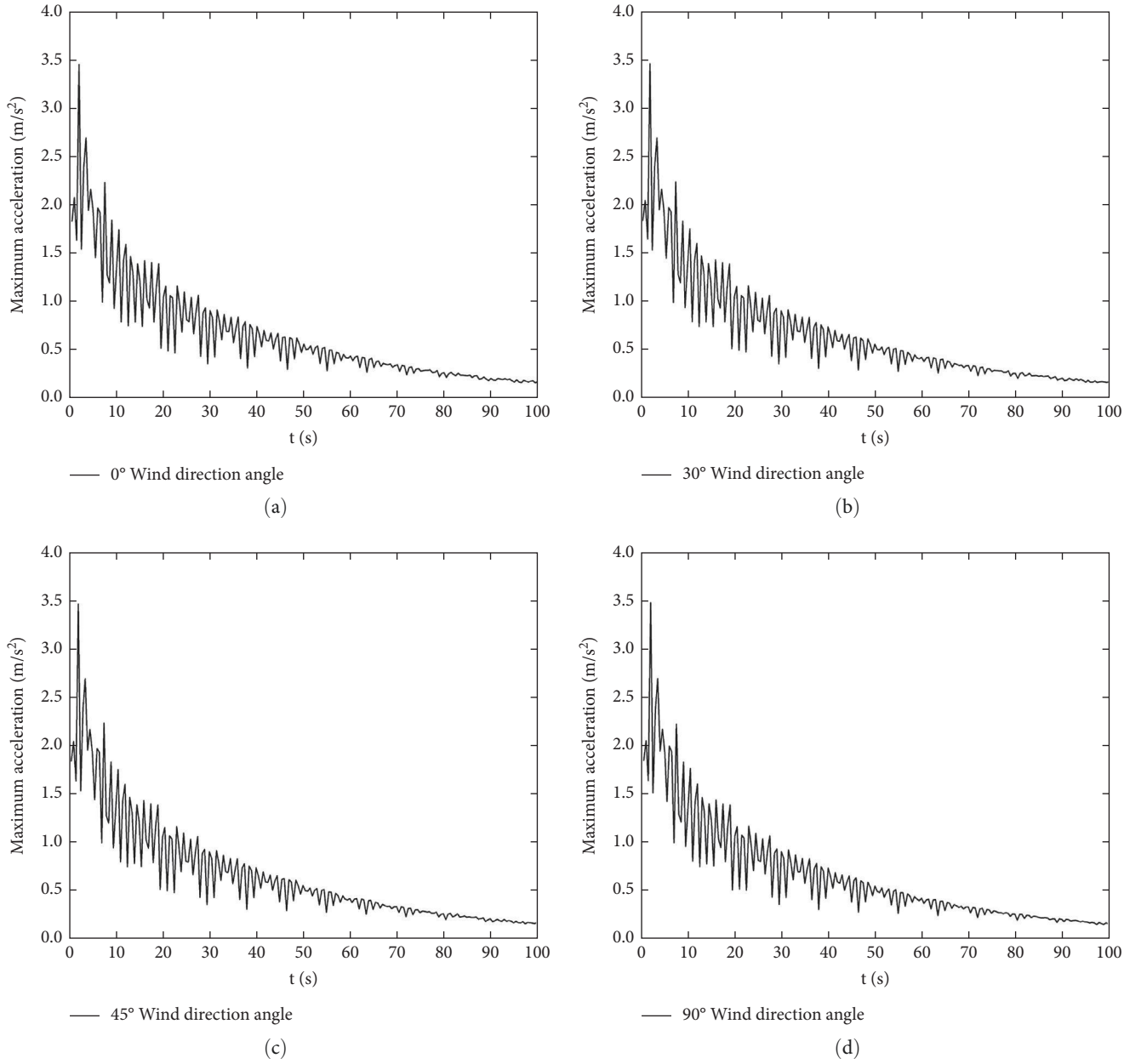

Figure 14: Curve of maximum acceleration of membrane structure. (a) 0° wind direction angle. (b) 30° wind direction angle. (c) 45° wind direction angle. (d) 90° wind direction angle.

and equivalent force values of the structure. The overall displacement, acceleration, and equivalent force values of the structure show a certain symmetric distribution. Table 4 shows the variations of the instantaneous maximum displacement, instantaneous maximum acceleration, and maximum equivalent force values for each wind direction angle. It can be seen that the difference between the values of different wind directions is not large, but also shows a certain law, the maximum instantaneous displacement, maximum instantaneous acceleration, and maximum equivalent force all reach the maximum at 30° and the minimum at 90°, which is consistent with the law of wind pressure polar difference and verifies the accuracy of the wind pressure analysis method above.

5. Conclusions

The analysis of the flow-solid coupling of large-span membrane structure shows that the bidirectional flow-solid coupling has better reliability for the calculation of large-span membrane structure; the vibration analysis of the bidirectional flow-solid coupling of large-span membrane structure provides reference and basis for the research and engineering

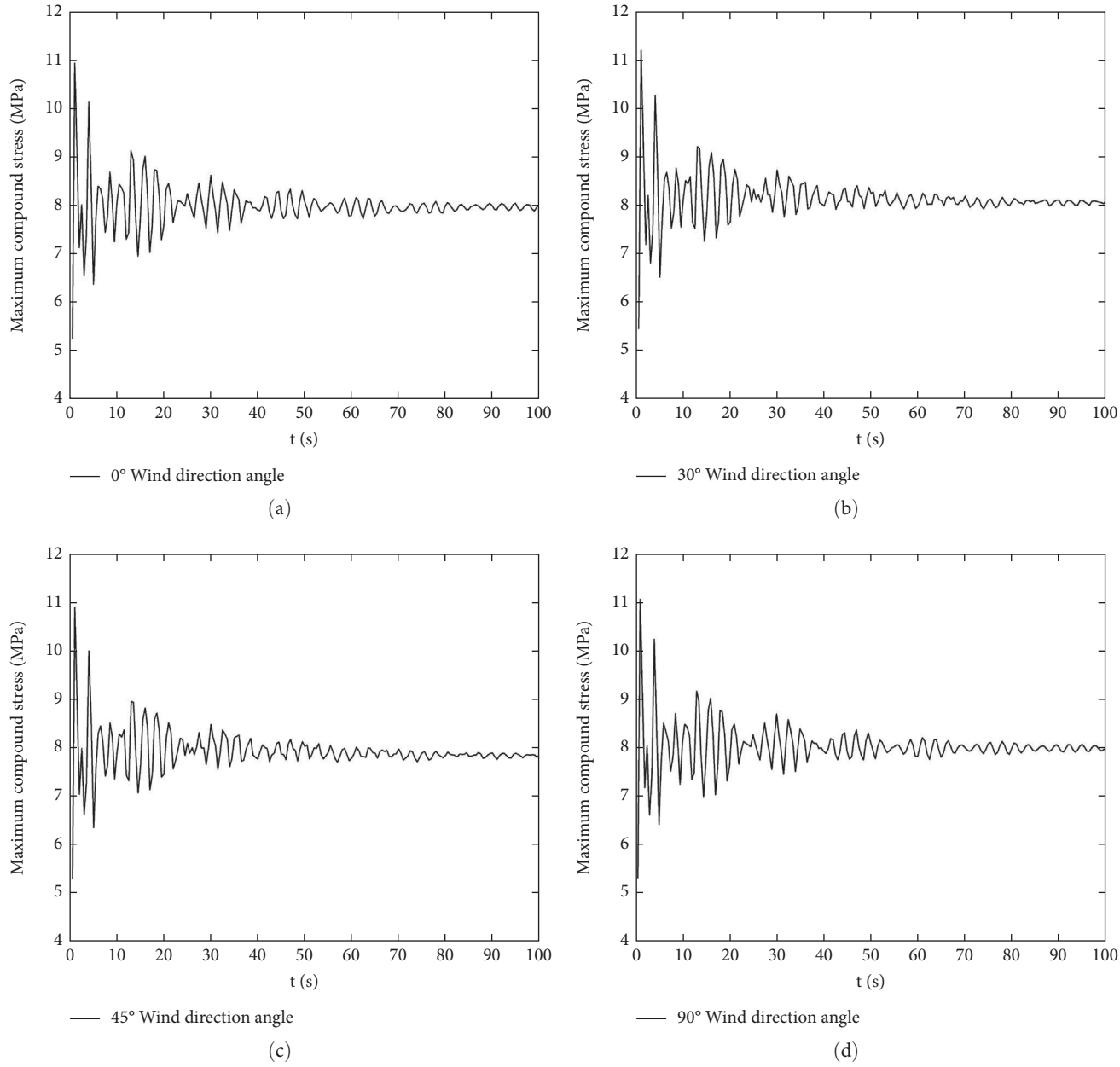

Figure 15: Diagram of time history curve of maximum equivalent stress of membrane structure. (a) 0° wind direction angle. (b) 30° wind direction angle. (c) 45° wind direction angle. (d) 90° wind direction angle.

application of this structure. The following conclusions are also obtained.

(1) For the complexity of the actual large-span membrane structure, the physical model is simplified using the modal-fitting method, and the modal frequencies of the 30th order are compared between before and after the model simplification are compared, and the maximum error is 5%, mode shapes is also fitting well, which makes the model have roughly the same stiffness before and after simplification, and provides an effective computational model basis for the wind-induced vibration analysis later.

(2) For the distribution of the averaged wind pressure coefficient on the membrane surface, comparing the polar difference of wind pressure coefficient can get the maximum wind angle 45° under unidirectional coupling, and the maximum wind angle 30° under bidirectional coupling; the overall polar difference of bidirectional coupling is greater than that of unidirectional coupling, considering the influence of membrane structure deformation on the flow field, which is more in line with the actual law and verifies the reliability of bidirectional coupling on the calculation of large span membrane structure; the analysis of the averaged wind pressure coefficient of key

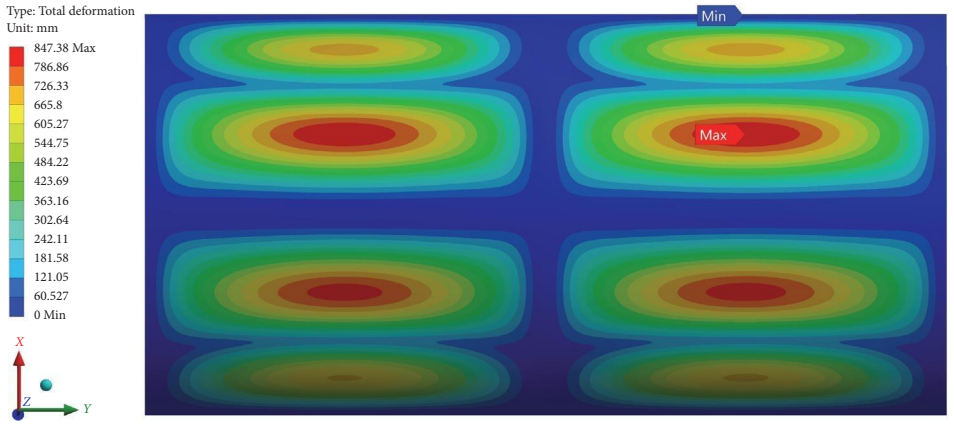

(a)

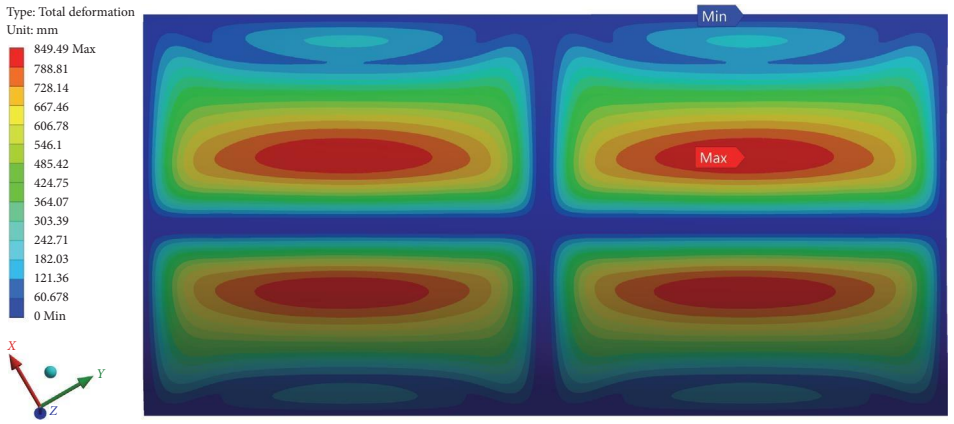

(b)

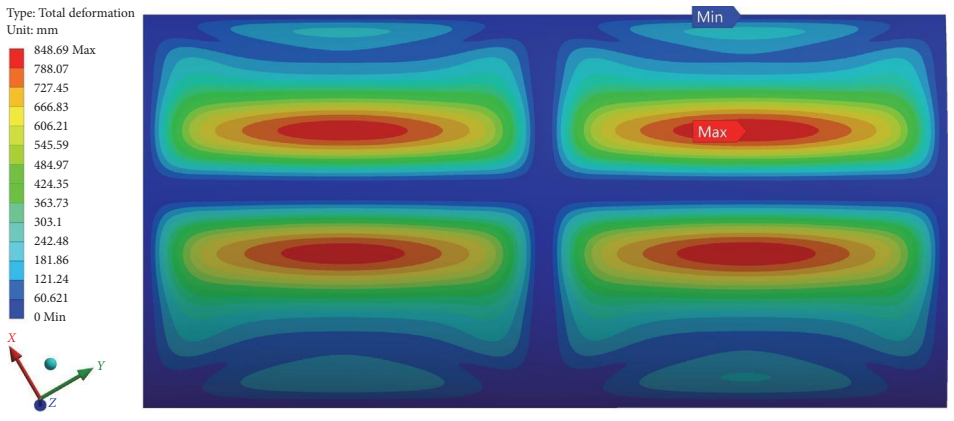

(c)

Figure 16: Continued.

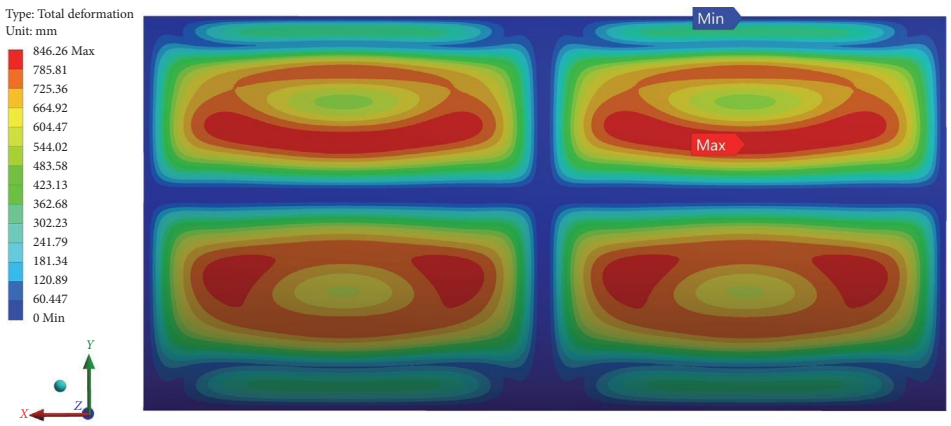

(d)

FIGURE 16: Diagram of maximum displacement of membrane structure (a) 0° wind direction angle. (b) 30° wind direction angle. (c) 45° wind direction angle. (d) 90° wind direction angle.

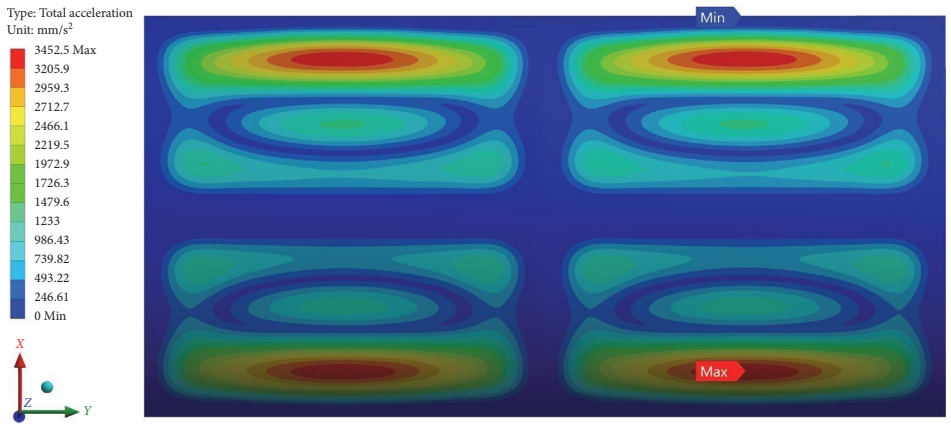

(a)

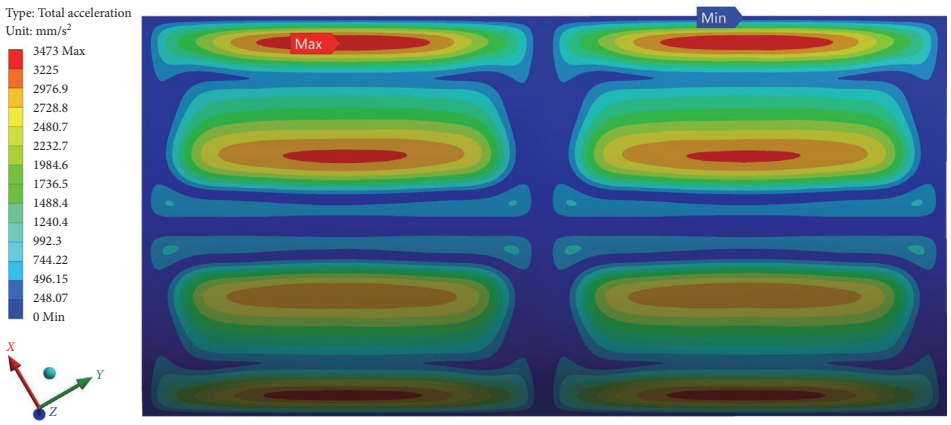

(b)

FIGURE 17: Continued.

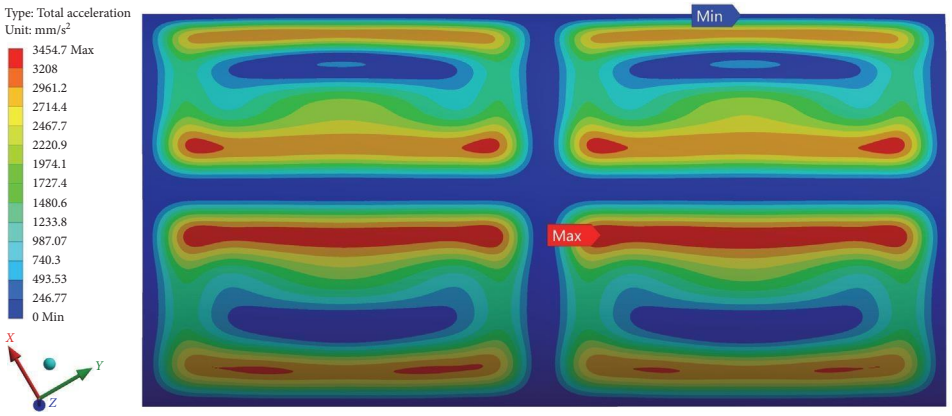

(c)

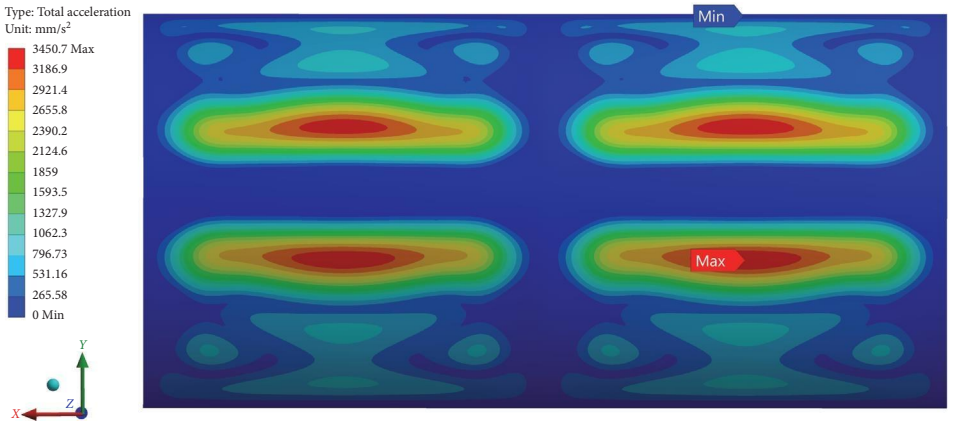

(d)

Figure 17: Diagram of maximum acceleration of membrane structure. (a) 0° wind direction angle. (b) 30° wind direction angle. (c) 45° wind direction angle. (d) 90° wind direction angle.

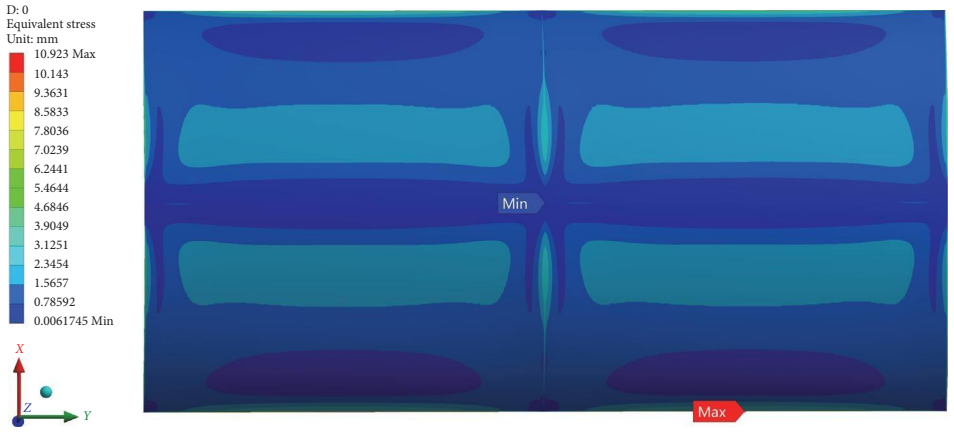

(a)

Figure 18: Continued.

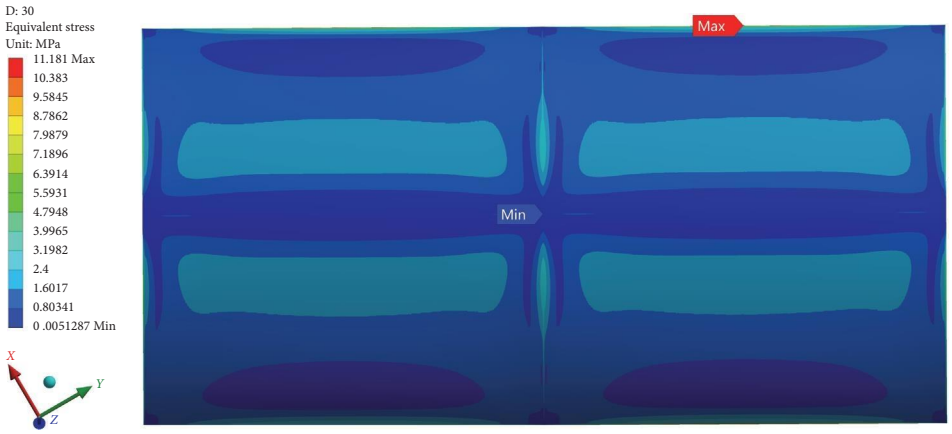

(b)

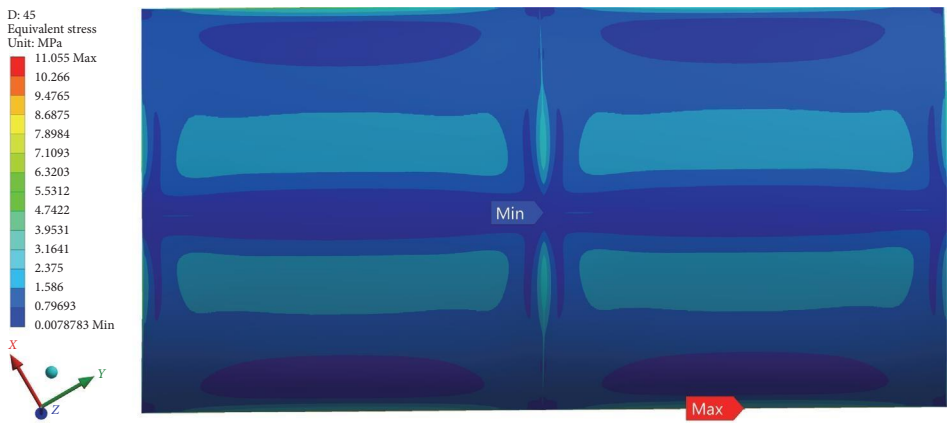

(c)

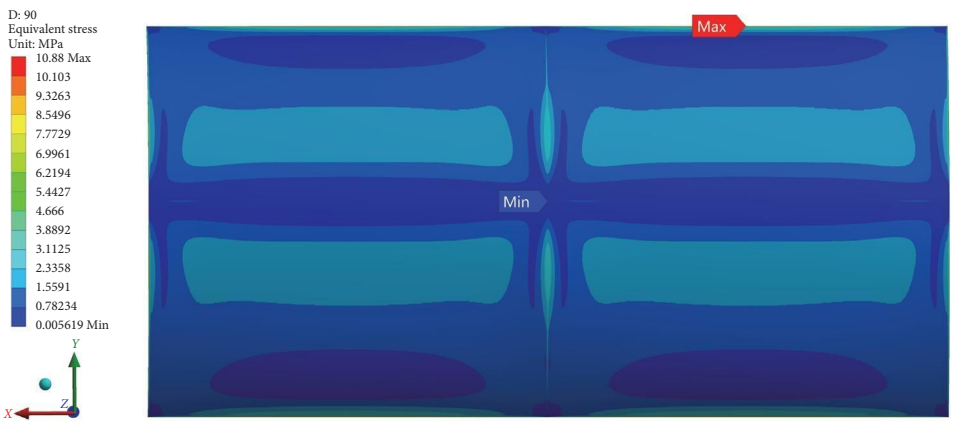

(d)

Figure 18: Diagram of maximum equivalent stress of membrane structure direction. (a) 0° wind direction angle. (b) 30° wind direction angle. (c) 45° wind direction angle. (d) 90° wind direction angle.

Table 4: Summary of maximum displacement and maximum acceleration at different wind angles under bidirectional coupling.

Wind angle	0°	15°	30°	45°	60°	75°	90°
Maximum instantaneous displacement (mm)	847.38	848.46	849.49	848.69	848.46	847.23	846.26
Maximum instantaneous acceleration (mm/s^2)	3,452.5	3,450.3	3,473.7	3,450.7	3,468	3,465.1	3,450.7
Maximum instantaneous equivalent force (MPa)	10.92	10.98	11.18	11.05	11.16	10.95	10.88

measurement points has obtained the unfavorable wind angle working condition from 0° to 45°.

(3) The trends of maximum displacement, compound stress, and maximum acceleration time course change curves for different wind angles are basically the same, the maximum displacement, maximum stress, and maximum acceleration are mainly reflected in the difference of different positions, which is consistent with the averaged wind pressure distribution; with time, the membrane structure appears to be in gradual equilibrium under the action of tension and stress; the instantaneous maximum displacement and instantaneous maximum acceleration, maximum compound stress all reach the maximum at wind angle 30° and the minimum at 90°, which is consistent with the law in wind pressure analysis.

(4) Considering that the overall stiffness of the structure is mainly affected by the rigid structure elements, whereas the stiffness of the membrane elements has little influence, the scaling ratio model is not made after simplification, which is limited to finite-element simulation. If a reasonable scaling ratio model with the same stiffness is calculated, the correctness of the wind-vibration response part can be further verified by comparative analysis between experiment and simulation.

Data Availability

In this paper, based on the article "Wind tunnel investigation on the wind load of large-span coal sheds with porous gables: influence of gable ventilation," numerical simulation is conducted to verify the correctness (https://sci-hub.st/10.1016/j.jweia.2020.104242).

Conflicts of Interest

The authors declare that they have no conflicts of interest.

Acknowledgments

This study was funded by the National Natural Science Foundation of China (51908108).

References

[1] Q. S. Yang, F. Tan, and X. F. Wang, "Loading and wrinkling analysis of membrane structures," *Science China Technological Sciences*, vol. 54, pp. 2597–2604, 2011.

[2] Y. Takadate and Y. Uematsu, "Steady and unsteady aerodynamic forces on a long-span membrane structure," *Journal of Wind Engineering and Industrial Aerodynamics*, vol. 193, Article ID 103946, 2019.

[3] W. Ding, "LES of unsteady aerodynamic forces on a long-span curved roof," in *Flight Physics: Models, Techniques and Technologies*, pp. 101–118, InTech, 2018.

[4] X. Wang, J. Ma, S.-S. Law, and Q. Yang, "Numerical analysis of wrinkle-influencing factors of thin membranes," *International Journal of Solids and Structures*, vol. 97-98, pp. 458–474, 2016.

[5] Q. Yang, T. Wang, B. Yan, T. Li, and M. Liu, "Nonlinear motion-induced aerodynamic forces on large hyperbolic paraboloid roofs using LES," *Journal of Wind Engineering and Industrial Aerodynamics*, vol. 216, Article ID 104703, 2021.

[6] T. Wang, K. Guo, Q. Yang, S.-S. Law, and X. Hu, "Estimation of wind-induced responses of large membrane roofs including the nonlinear motion-induced aerodynamic forces," *Journal of Wind Engineering and Industrial Aerodynamics*, vol. 227, Article ID 105053, 2022.

[7] B. Y. He, S. X. Wang, G. G. Jin, and H. Wang, "Dynamic model of a moving flexible camber beam by the method of fitted modal," *Journal of Astronautics*, vol. 24, no. 3, pp. 273–277, 2003.

[8] X. Wu, Y. Lei, and D. Li, "Dynamic analysis of a large scale satellite structure with the liquid propellant consuming," *Journal of National University of Defense Technology*, vol. 34, no. 4, pp. 38–42, 2012.

[9] C. E. N. Mazzilli, P. B. Gonçalves, and G. R. Franzini, "Reduced-order modelling based on non-linear modes," *International Journal of Mechanical Sciences*, vol. 214, Article ID 106915, 2022.

[10] Y. Pan, M. Rao, Y. Zhou, S. X. Wang, and Y. J. Lin, "Study on membrane structural vibration frequency under fluid-structure coupling," *Journal of Building Structures*, vol. 40, no. 8, pp. 136–144, 2019.

[11] Y. Zhang, Q. Zong, R. Q. Liu, C. Shi, and Q. H. Lin, "Study of coupled dynamics of planar thin film structures with dimensionless analysis," *Journal of Vibration Engineering*, vol. 35, no. 2, pp. 495–502, 2022.

[12] J. Rong, Z. Liu, P. F. Xin, D. L. Xiang, and Z. P. Wu, "Simulation analysis of coupled dynamics of a typical thin film space structure," *Journal of Beijing University of Technology*, vol. 38, no. 4, pp. 347–352, 2018.

[13] Y. Wu, Z.-Q. Chen, and X.-Y. Sun, "Research on the wind-induced aero-elastic response of closed-type saddle-shaped tensioned membrane models," *Journal of Zhejiang University-SCIENCE A*, vol. 16, pp. 656–668, 2015.

[14] F. Sun, H. Tang, M. Lu, D. Zhang, and C. Lu, "A study on wind pressure characteristics of a large-span membrane structure under the fluctuating wind in a vertical direction based on a large eddy simulation," *Modelling and Simulation in Engineering*, vol. 2022, Article ID 8209487, 12 pages, 2022.

[15] F. Sun, D. Zhu, T. Liu, and D. Zhang, "Study on fluid-structure interaction of flexible membrane structures in wind-induced vibration," *Shock and Vibration*, vol. 2021, Article ID 8890593, 10 pages, 2021.

[16] B. Wang and Q. Yang, "Implementation and application of weakly coupled algorithm," *Engineering Mechanics*, vol. 25, no. 12, pp. 48–52+59, 2008.

[17] M. X. Chen, W. C. Jia, and D. Yang, "Comparative study of cantilevered flat plate winding vortex vibration characteristics based on unidirectional solution and bidirectional fluid-solid coupling," *Ship Mechanics*, vol. 24, no. 1, pp. 70–78, 2000.

[18] D. Lu, W.-J. Lou, and Y. Yang, "Numerical calculation on wind-induced damping of membrane structure based on fluid–structure interaction," *Zhendong yu Chongji (Journal of Vibration and Shock)*, vol. 32, no. 6, pp. 47–53, 2013.

[19] F.-J. Sun and M. Gu, "A numerical solution to fluid-structure interaction of membrane structures under wind action," *Wind and Structures*, vol. 19, no. 1, pp. 35–58, 2014.

[20] Ministry of Housing and Urban-Rural Development of the People's Republic of China, "GB 50009-2012 code for structural loads on buildings," China Construction Industry Press, Beijing, 2012.

[21] China Engineering Construction Standards Association, "Technical regulations for membrane structures CECS158:2015," China Planning Press, Beijing, 2015.

[22] National Standard, ""Steel Structure Design Standard" GB50017-2017 officially released," *China Building Metal Structure*, vol. 434, no. 2, Article ID 72, 2018.
[23] Y. Wu, Y. Sun, C. Zheng, and X. Y. Sun, "Wind engineering and structural wind resistance design," Harbin Institute of Technology Press, Harbin, 2019.
[24] Y. Shen, Y. Li, C. Liu, and J. Wang, "Study on wind pressure distribution of truncated ellipsoidal inflatable membrane structure considering fluid-solid coupling and pulsating wind effect," *Industrial Building*, vol. 52, no. 6, pp. 120–126, 2022.
[25] B. Zheng, "Preliminary study on numerical Wind Tunnel Simulation based on ANSYS," Beijing Jiaotong University, 2008.
[26] Y.-F. Sun, L.-J. Z, Q.-K. Liu, X.-B. Liu, and W.-Y. Ma, "Study on the influence of closed form on wind load of long-span coal shed," *Engineering Mechanics*, vol. 36, no. S1, pp. 234–239, 2019.
[27] N. Su, S. Peng, N. Hong, and T. Hu, "Wind tunnel investigation on the wind load of large-span coal sheds with porous gables: influence of gable ventilation," *Journal of Wind Engineering and Industrial Aerodynamics*, vol. 204, Article ID 104242, 2020.